文章编号：0258-7025(2009)12-3149-11

Laser Welding, Microwelding, Nanowelding and Nanoprocessing

(Invited Paper)

A. Hu[1] S. K. Panda[2] M. I. Khan[1] Y. Zhou[1]

[1] *Department of Mechanical and Mechatronics Engneering, University of Waterloo, 200 University Avenue West, ON, N2V 2V6, Canada*

[2] *Department of Mechanical Engineering, Indian Institute of Technology-Kharagpur, Kharagpur 721302, India*

Corresponding author: a2hu@uwaterloo.ca

Received October 13, 2009

Abstract Laser has been widely applied for advanced material processing, such as welding of advanced high strength steels (AHSS) for automotive applications and Pt, Ti, and Nitinol alloys for medical applications. Recently, ultrafast pulse laser, especially femtosecond laser, is identified as powerful tools for joining and surface engineering of nanomaterials. This paper reviews our research on these fields at the Centre of Advanced Materials Joining, University of Waterloo. Representative conclusions are listed for laser material processing at three continuing scales. 1) For AHSS welding, a thin Al layer can dramatically enhanced the weldability of galvannealed AHSS. The movement of the welding line and softening in the vicinity has significantly influence on global mechanical properties in dual phase (DP) and transformation induced plasticity (TRIP) steels. The increase of the strength ratio decreases the formability and results in the non-uniform strain distribution. 2) For medical micro-welding, oxygen is found to be a key role for welding strength and microstructure. The formation of intermetallics reduces the relative ductility and increases the susceptibility of cracking. Different laser processing parameters can significantly influence weld mechanical performance. 3) For femtosecond laser nanofabrication, the joining of Au nanoparticles is successfully achieved by controlling laser energy. Surface nanostructure of Ag induced by femtosecond laser irradiation can work effective probes for surface enhanced Raman spectroscopy.

Key words laser welding; nanofabrication; mechanical property; advanced materials; medical application

CLCN: TV547.6 **Document Code**: A **doi**: 10.3788/CJL20093612.3149

1 Introduction

Welding and joining is an essential step for various device manufacturing at all scales, spanning from macro, micro, to nano[1]. Welding covers the fusion of two substrates by melting the surface so that an external energy source is required. Laser, a stimulated and intense emission of radiation, is widely employed for welding because it provides a non-contact and fast processing. This allows complicated three-dimensional (3D) welding and the operation at different temperature, pressure, and mediums (vacuum, air, or even aquatic environments). Since the intense light beam can be focused to a very small size, laser welding enables precisely-controllable micro-sized joining. However, when the building blocks further shrink into submicrometer or even to a range of nanometers, such as, for the fabrication of nanomechancial engineering systems (NEMS), the melting has to be controlled within a thickness of a few or tens nanometers. Ultrafast pulsed laser is an innovative tool in this field for nanoscopic processing[2]. Femtosecond laser irradiation can result in an ultrafast and nonthermal melting of solid materials, which is promising for developing novel joining technologies for nano and/or molecular devices. With the explosive development of nanoscience and technology, nanoscopic joining technologies are gaining more and more significances[3].

In recent years, there is growing interest for application of low carbon advanced high strength steels (AHSSs) in tailor welded blanks (TWBs) to address the objectives of decreased body in white weight and improved crashworthiness. The multiphase AHSSs (like dual phase (DP) and transformation induced plasticity (TRIP) steels) have superior combinations of strength and formability, while being reasonably simple and inexpensive to manufacture[4]. To enhance corrosion resistance and dura-

Partially supported by the National Centre of Excellent (NCE) through Auto21, Natural Science and Engineering Research Council (NSERC) of Canada and the Canada Research Chair (CRC).

bility, these automotive grade steel sheets are zinc coated, usually galvanized or galvannealed[5]. Two or more AHSS sheet shapes with different strength, thickness, and/or coating characteristics can be joined together to create a blank, which is so called TWBs with engineered properties[6]. Although TWBs have been made by using different types of welding techniques, the most common method currently in use is laser beam welding[6]. The quality and properties of the weldment (fusion and heat affected zone (HAZ)) in a TWB are critical for a successful forming operation[7~9]. One of the major issues on weldability of galvanized and galvannealed AHSS is the porosity due to boiling of Zn, which has a lower boiling point (906 ℃) compared with the liquidus temperature of low-carbon steels (1530 ℃), and hence, develops high Zn vapor pressure during laser welding. Researchers have worked on various ways to reduce Zn vapor pressure by combining Zn with another substance: addition of iron oxides to the faying surface region[10], addition of oxygen to the inert shielding gas environment surrounding the weld[11], interfacial addition of copper[12], etc. However, all these approaches are not without inherent problems in terms of oxidation-related physical and chemical changes to the weld itself, and copper is also a problematic addition because it promotes solidification cracking of steel[13]. Another issue is change in mechanical and metallurgical properties of the weldment. Hence welding techniques and weldability of different grades, thicknesses, and zinc coatings of AHSS sheets, and optimization of the weld parameters for getting sound weld by proper inspections and testing techniques are reviewed in this paper. Some of the above issues for DP and TRIP steels are also addressed.

Laser welding is commonly implemented in miniature applications, due to its ability to create small scale joints. In particular the pulsed Nd:YAG process enables high local energy densities with minimal heat inputs, producing welds with minimal heat affected regions. However, certain challenges have been faced while implementing the pulsed Nd:YAG process for medical device applications, particularly in contamination due to shielding[14], intermetallic formation[15], and a reduction in mechanical properties[16]. The currents article details these issues by reviewing several case studies.

Various nanojoining approaches have been developed, including e-beam exposure[17], focusing ion beam deposition[18], ultrasonic welding[19], sputtering/evaporating Au and post-annealing[20,21], and nanosoldering with low melting point solders[22,23]. Recently, nanowelding of Au nanoparticles has been displayed by irradiation of Au solution by picosecond laser pulses[24]. Nanowelding leads to the formation of metallic connection between noble metallic nanoparticles. Our study displays that the welded Au nanoparticles can work effectively for surface enhanced Raman spectroscopy[3,25]. Besides, we observe that direct irradiation of Ag foil can induce nanopatterns on the surface. These nanostructures can also work for the probe of surface enhanced Raman spectroscopy. This paper reviews current progress in nanojoining using femtosecond laser welding and femtosecond laser surface processing. Both processes have potential for high sensitive molecular analysis and detections with surface enhanced Raman spectroscopy.

2 Experiment

2.1 Weldability of Galvannealed AHSS

Investigation of weldability of Zn coated dual phase steel sheets (with tensile strength of 600 MPa, thickness of 1.00 mm, and 45-gm/m^2 zinc per side) and interfacial addition of Al for process stabilization was carried out by test-welding small lap joint assemblies, generally by using pairs of rectangular coupons approximately 40 mm × 100 mm in size inserted in a bolted fixture capable of applying high clamping loads[11]. Welding was carried out using two laser systems (a 4-kW direct diode laser and a 3-kW Nd:YAG) with the beam focal plane at the top surface of the lap assembly and flowing argon at 14 L/min on the top surface for shielding.

2.2 Metallurgical and Mechanical Properties of AHSS-Weldment

Various advanced high strength steel materials like DP450, DP600, DP980, Al-alloyed TRIP, and Si-alloyed TRIP steels were butt welded using proper laser power and welding speed in both the above laser welding system[12,13,26~28]. The weld fusion zone and HAZ microstructure were observed under optical and scanning electron microscope (SEM). Microhardness indentation across the weld was carried out at a load of 500 gm and tensile tests of welded coupons were conducted at room temperature.

2.3 Formability of Laser Welded AHSS Blanks

Formability of laser welded AHSS blanks of similar and dissimilar material combinations was evaluated by Hecker's limiting dome height (LDH) test using 101.6-mm diameter hemispherical punch[29~32]. Finite element simulations of the forming test were done by using LSDYNA-971 commercial available software package to evaluate the affect of weld zone and difference in material properties on LDH, fracture location, strain distribution, and weld-line movement[31,32].

2.4 Microwelding

The weld experiments described in the current review were conducted using a pulsed Nd:YAG laser welding system with a 1.06 μm wavelength. Specifications of testing methods can be found in Refs. [14~16].

2.5 Nanojoining and Surface Processing

Femtosecond laser welding and surface irradiation were carried out with a 100-fs 800-nm Ti:sapphire laser system with a pulse energy of 300 μJ/pulse and repeatition rate of 1 kHz[33]. Au nanoparticles were synthesized by the citrate redution of $HAuCl_4$. Welding was done in liquid by focusing the laser into a quatz cell or in solid by depositing Au nanoparticles onto a TEM Cu-grid. For surface processing of silver, silver pellet was first mechanically polished to 0.3 μm and then cleaned in ultrosonic base with acetone.

3 Results and Discussion

3.1 Effects of Interfacial-Al on Weldability of Galvannealed AHSS

Figure 1(a) illustrates severe porosity of a weld made using galvannealed DP600 material. A comparable weldment of the same material made with addition of 25- μm thick commercial pure Al-foil at the interface of lap-joint is shown in Fig. 1(b). Surfaces of finished welds typically showed some evidence of some minor weld pool instability, but the type of gross expulsive porosity that was characteristic of such welds was virtually eliminated when Al foil was present. Shear testing of these initial welds served to confirm the practical benefits of the Al addition in terms of increased joint strength, as shown in Fig. 1(c). Coupon examination after mechanical testing showed that the strength increase resulted directly from increased nugget shear area, due both to the absence of gross fusion zone porosity and a general increase in weld penetration, due to the improved thermal contact between lapped sheets afforded by the presence of

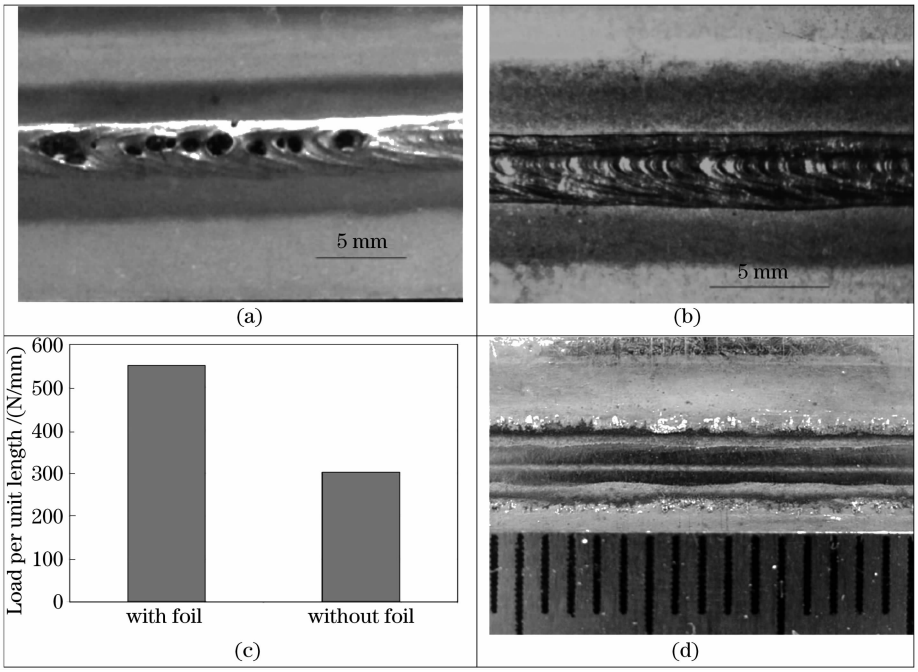

Fig. 1 Effects of interfacial aluminum addition on surface appearance and strength of lap welded galvannealed DP600 steel. (a) typical severe porosity due to zinc vapor evolution (without Al foil); (b) surface without gross expulsive porosity when 25-μm Al foil was used at interface (4-kW diode laser and welding speed of 0.7 m/min); (c) shear testing results of lap welds with and without 25-μm Al foil; (d) surface of diode laser lap weld on Al spray coated steel sheets (welding speed of 0.55 m/min)[11]

the interfacial Al film. In the early development work, the use of inserted aluminum foil reduced but in some cases did not completely eliminate the welding process instability. It was theorized and has subsequently been determined that this resulted from inconsistent contact between the work pieces and foils, leading to the inconsistent interaction between Al and Zn in the crevice. Recognizing the importance of local fit up, systematic studies were done further on process stability improvements with adding Al as a cold spray-coating on the galvanized steel surface prior to joint assembly. This process appeared to be potentially very appropriate for applying small amounts of Al to galvanized surfaces, since it operates at moderate temperature thus avoiding melting or excessive oxidation of particulate or work pieces. Coated steel coupons were assembled together in pairs, clamped together and welded with the diode laser. Finished welds displayed excellent process stability and complete freedom from vapor-induced weld pool disruption or porosity. Typical surface appearance of these welds is illustrated in Fig. 1(d). Weld cross sections showed excellent mixing of Al and Zn liquids in the crevice, but they also showed a tendency to excessive dissolution of Al into the steel weld beads (i. e., the presence of some delta ferrite in the weld metal indicated Al pickup of about 1%～1.5% by weight). Additional test welds were therefore carried out by using the available set of coated coupons, reducing the quantity of Al present in the crevice of 50% by pairing coated and uncoated coupons[11]. These welds also displayed stable process operation and freedom from Zn-induced porosity together with much lower weld bead Al pickup.

3.2 Metallurgical and Mechanical Properties of AHSS Weldment

3.2.1 Dual Phase Steels

The microhardness profile obtained across the laser butt weldment of different dual phase steel indicating base metal, HAZ, and fusion zone is shown in Fig. 2(a)[12]. It was found that the laser type and base material affect the weld hardness profile (Nd: YAG laser and DP980 steel produced harder weld). The micro structure of fusion zone consists of mainly martensite. Just outside the fusion zone and near the fusion boundary, the peak temperature exceeds the critical temperature upon which 100% austenite forms (Ac3). This region is called the supercritical HAZ. Further from the fusion boundary, the peak temperature is within the intercritical range, which results in austenitization of the carbon-rich martensite phases while large areas of undissolved ferrite remain unchanged. For transformable steels including DP, the cooling rate is largely dependent on the welding heat input (in the range which austenite decomposes to the final room temperature microstructure), and is a critical determinant of the phases present. In laser welding of DP steels, the cooling rate is typically high enough to result in the decomposition of austenite to hard metastable phases such as martensite, bainite, and carbides. Thus, the room temperature microstructures of the fusion zone and the inner-HAZ (consisting of the supercritical and intercritical regions) consist of a higher volume fraction of hard phases than the base metal with a resultant increase in microhardness and together form a "hardened zone". Further from the fusion boundary the peak temperature is below Ac1, the temperature where austenite transformation begins (i. e., subcritical); however, tempering of the metastable martensite phase occurs, resulting in an overall reduction in microhardness. This outer-HAZ forms a "softened zone," which is adjacent to the unaffected base metal[28]. It was also found that both the laser type and material affected softening behavior: the welds made with Nd: YAG laser only DP980 exhibited softening, however all the materials welded with diode laser softend to various degree at the outer-HAZ (7 VHN for the DP450, 18 VHN for the DP600, and 50 VHN for the DP980)[12]. The comparison of microstructure of various regions (base metal, softened outer-HAZ, and the fusion zone) of a DP980 steel sheet is shown in Figs. 2(b), (c), and (d)[30]. It was observed that the extent of softening and the width of softened outer-HAZ in DP980 steel sheet were greatly affected by laser power and welding speed. During transverse tensile testing of laser welded DP980 steel, failure occurred by ductile rupture due to strain localization in the outer-HAZ resulting in lower ultimate tensile strength compared with base metal. The finite element (FE) simulation was able to predict the mechanical properties of the soft zone and fracture location during tensile test (Fig. 2 (e))[28]. FE results showed that the strength of the joint decreased significantly with the formation of a softened zone. As the strength of the softened zone

decreased, the strength of the joint decreased as well. Numerical results also showed that increasing the width of the softened zone with a constant strength would result in a decrease in the overall joint strength, while the elongation was unaffected.

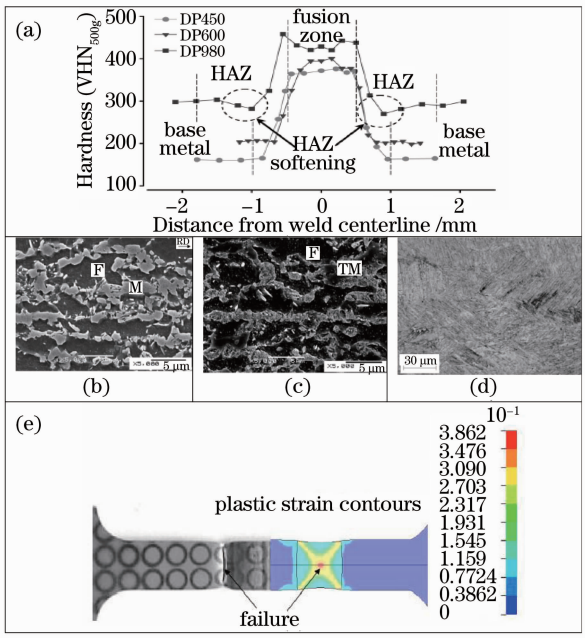

Fig. 2　Effect of laser welding on DP steel. (a) microhardness across the weldment (3-kW Nd:YAG laser welding at 6.0 m/min)[12]; (b), (c), and (d) microstructures of base metal, outer-HAZ, and fusion zone (in DP980)[30], respectively; (e) failure at the outer-HAZ of a DP980 transverse welded tensile sample[28]

3.2.2　TRIP Steels

The weldment microhardness distribution of the Si- and Al-Trip steel (with a welding speed of 1.6 m/min) is shown in Fig. 3(a), in which 251 HV and 221 HV are the base metal hardness values for Si- and Al-alloyed steels, respectively[13]. The difference in base metal hardness is believed to result mainly from the chemistry difference even though the steels have similar carbon equivalent, for that Si is a very effective solid-solution strengthening element in the ferrite phase. As shown in Figs. 3(b) and (c), both base metal microstructures are composed of polygonal ferrite (grey), bainite (black), and retained austenite (white). The area fraction of retained austenite in the Al-alloyed steel is about 13%, a little bit higher than that in the Si-alloyed steel of about 12%. In the weld fusion zone, the hardness of the Si-alloyed steel is far above that of the Al-alloyed steel and this is due to the fundamental differences in weld microstructure between the steels. The fusion zone of the Si-alloyed steel is composed essentially entirely of a single phase of martensitic morphology, as shown in Fig. 3(d) (measured fusion zone hardness of 484 HV). In contrast, the Al-alloyed steel fusion zone comprises a multiphase microstructure as shown in Fig. 3(e) and the experimental fusion zone hardness (331 HV) is below fully martensitic structure. It is well known that Al is a strong ferrite stabilizer and can promote high temperature ferrite as the primary phase in the solidification process. In TEM observation of welds in the Al-alloyed steel, two kinds of retained austenites were observed in the fusion zone. One was austenite films between bainitic ferrite laths and the other

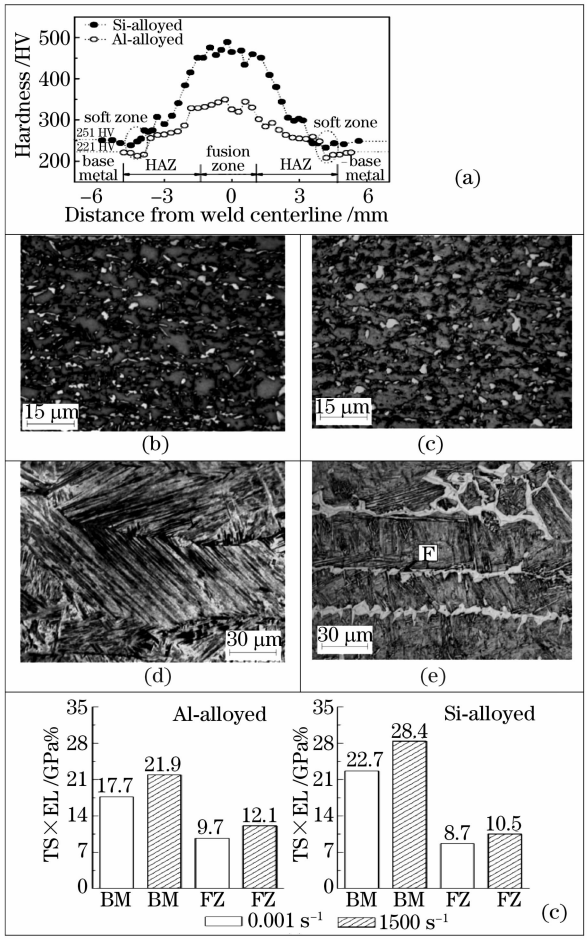

Fig. 3　Effect of laser welding on TRIP steel. (a) microhardness across the weldment (4 diode laser welding at 1.6 m/min)[13]; (b) and (c) microstructure of Si and Al-alloyed TRIP steel; (d) and (e) microstructure of Si- and Al-alloyed TRIP steel fusion zone (diode laser welding)[13]; (f) strength ductility balance of base metal and fusion zone at different strain rates[13]

morphology was chunk shaped austenite occasionally observed dispersed in the ferrite matrix. The retained austenite can be attributed to the role played by the Al in suppressing the carbide precipitation[13,26,27]. Also the presence of the retained austenite is expected to enable the fusion zone have the TRIP effect by transforming to martensite on straining and contributes to uniform elongation, which is desired in TRIP steel welding in order to achieve matching properties with base metal. Outside the fusion zone, hardness decreases gradually to the base metal level. Soft zones are also observed in the outer HAZ for both the welded TRIP-steels. Figure 3(f) shows the effect of strain rate on strength and ductility of base TRIP steel and welded zone. It is found that the Si-alloyed base metal shows a better combination of strength and total elongation than that of the Al-alloyed steel at corresponding strain rates. The difference was explained above. After welding, fusion zones for both steels show a marked decrease of strength-ductility balance. This means that the welding process has a detrimental influence on the steels' formability behavior. But the Al-alloyed fusion zone has a lower decrease (45.1%) than that of the Si-alloyed steel (62.9%) at the quasi-static strain rate. The decrease is also similar for the dynamic tensile tests, although strain rate-induced increases in strength lead to higher strength-ductility balances.

3.3 Formability of Laser Welded Blanks

Figure 4(a) shows significant reduction in LDH (approximately 57%) for diode laser welded DP980 steel sheet compared to monolithic DP980 steel sheet[29]. In DP welded specimens, the fracture path was always entirely in the outer HAZ[30]. FE analysis with incorporation of fusion zone and HAZ properties showed that strain was localized at the softzone during stretch forming of DP980 welded blank and with further deformation fracture mode close to plane strain condition taking place at outer HAZ[32]. The LDH of the formability of a welded dual phase (980 MPa) blank that exhibits a soft zone depends on the nature of the flow properties (both K and n values) of the soft zone compared with the base metal. Similar decrease in LDH and strain localization at the outer HAZ was observed in the welded DP800 steel (Fig. 4(b))[31]; however, when these materials were combined with the lower strength HSLA, strain and failure were localized in

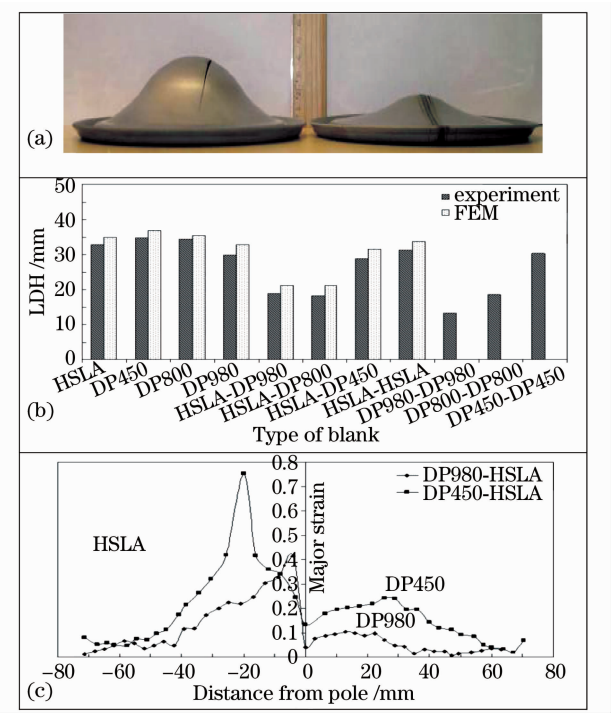

Fig. 4 Formability of laser welded blank. (a) biaxial stretch formed DP980 laser welded blank and monolithic unwelded DP980 blank[29]; (b) comparison of LDH of parent metals and diode laser welded blanks obtained from experiment and FEM simulation[31]; (c) comparison of strain distribution on two deformed TWBs of dissimilar material combination[31]

the HSLA side of the TWB. This was due to the higher strength and hardness of the soft zone compared to that of the HSLA base metal, which caused strain localization to shift from soft zone to HSLA side (Fig. 4(c)). Non-uniform deformation with movement of weld line towards the stronger side was observed during stretch forming of dissimilar material welded blanks, which decreases the LDH compared with parent monolithic blank. Figure 4(c) shows a comparison of the major strain distribution patterns for the HSLA-DP980 and HSLA-DP450 combinations. For the stronger side (i.e., DP450 and DP980), there was more deformation in the HSLA-DP450 combination compared with the HSLA-DP980 combination. Thus, there was more non-uniform deformation and early strain localization close to the weld when HSLA was combined with higher strength metals, like DP980 or DP800. Hence it was observed that LDH, weld line movement, and fracture location during stretch forming of tailor welded blank depended on a non-dimensional parameter "strength ratio (SR)". Increased

strength ratio decreased formability and increased weld line movement, and resulted in non-uniform strain distributions[31].

3.4 Oxygen Contamination

Typically medical device materials are corrosion resistant and biocompatible while having unique mechanical properties. Examples of these materials include stainless steel, titanium, nitinol, and platinum alloys. However, these intrinsic properties often pose challenges and can be altered during fabrications processes, in particular during fusion welding processes such as pulsed Nd:YAG laser welding. The following section describes the common challenged occurred during laser micro welding of medical device materials.

Titanium's affinity towards oxygen plays a key role in its excellent corrosion resistant properties. However during welding oxide entrapment has shown to reduce mechanical performance and substantially increase weld metal hardness. Li *et al.* studied the effect of varying oxygen content in argon gas on the surface color and weld performance[14]. In practice, the surface color is the first indication of issues with oxidation contamination. It was observed that increasing oxygen content could result in a color change from a straw (less than 2% oxygen) to a purple/blue (near 5% oxygen) and finally a solid blue (10% or more oxygen). Similarly, the mechanical performance was also altered with the addition of oxygen, as shown in Fig. 5. Weld metal hardness increased from nearly 200 HV to about 300 HV when increasing oxygen from 0% to 10%. However the weld strength initially showed a slight increase up to a oxygen content of 2%, followed by a gradual decreased going below base metal strength at 10% oxygen content. Microstructure changes were also observed with oxygen free weld metal showing a mainly serrated alpha structure while contaminated weld metal exhibited acicular and platelet alpha. Hence, the structure and properties of weld metal can be greatly influenced by oxygen content.

3.5 Formation of Intermetallic Phases

Various materials are often implemented in medical device applications, which often required dissimilar joint combinations. Joining dissimilar materials typically results in the formation of undesirable intermetallic, particularly in processes where liquidus temperatures are surpassed. For example,

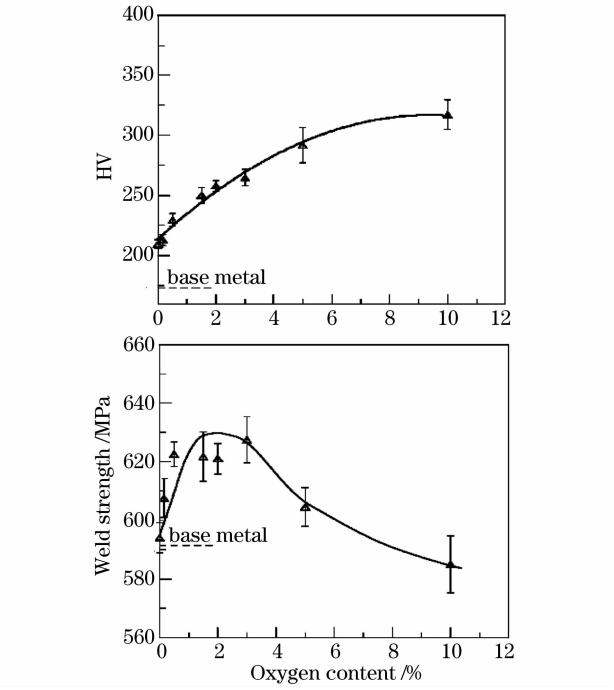

Fig. 5 Effects of oxygen content on weld strength and hardness

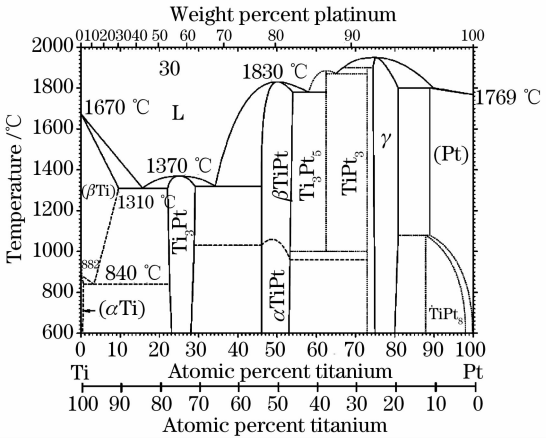

Fig. 6 Binary phase diagram showing the possible phases between Pt and Ti[34]

Noolu *et al.* studied the laser weldability of Pt and Ti alloys[15] that are commonly implemented in medical device applications. From simply observing the Ti-Pt phase diagram, as shown in Fig. 6[34], it is clearly shown that various intermetallic phases (Ti_3Pt, TiPt, Ti_3Pt_5, $TiPt_3$, etc.) can form between elemental titanium and platinum.

Figure 7(a) shows the backscattered electron microscope images of dissimilar Pt-Ir and Ti -6Al-4V Nd:YAG welds studies by Noolu *et al.*[15]. Weld metal primarily consisted of two structures which include the Ti_3Pt + TiPt eutectic where 67% Ti was observed and a primary TiPt with Ti_3Pt + TiPt eutectic for regions of containing 60% Ti. Hardness

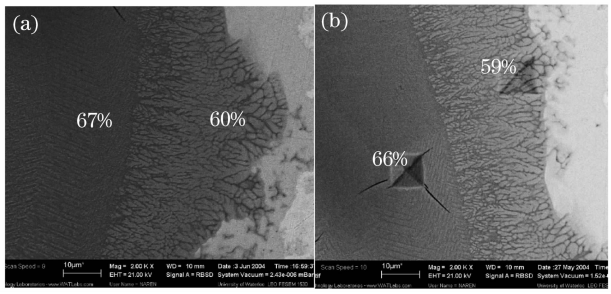

Fig. 7 Back scattered electron microscope images of weld metal microstructure and corresponding Ti content

values for the commercially pure Pt and Ti alloys are typically 40 and 160～220 HV, however the formation of the intemetallics resulted in a drastic increase ranging 400～700 HV. Furthermore, the known susceptibility for cracking of the Ti_3Pt was observed during hardness indentation of the 67% Ti regions, as shown in Fig. 7(b). Hence, the formation of intermetallics during Nd:YAG laser welding of Pt and Ti alloys have shown to substantially reduce the relatively ductility and increase the susceptibility for cracking.

3.6 Effects of Process Parameters on Mechanical Properties

The various process parameters associated with Nd:YAG laser welding (i.e., peak power, pulse frequency, and pulse time) can greatly influence the structure and properties of welds. Advanced medical device materials have unique mechanical properties, such as the pseudoelasticity exhibited by Nitinol alloys. In most applications Nitinol functions within the pseudoelastic range, which nicely mimics biological elements such as bone and tissue. However an investigation by Khan *et al*. revealed that process parameters could greatly affect the mechanical performance[16]. Figure 8 shows the stress-strain curve for the base material and select NiTi weld conditions. The base material exhibits initial elastic loading of the austenite phase followed the pseudoelastic plateau, up to 10% strain, where austenite transforms into martensite. Beyond the pseudoelastic region elastic, plastic deformation of martensite occurs until finally failing near 90% strain and 800 MPa failure load. Welding parameters clearly influenced the mechanical performance of welds. The 0.6-kW, 10-pps weld failed prior to reaching the pseudoelastic range on the graph. In contrast the 0.6-kW, 1-pps weld exhibited the pseudoelastic properties and achieved a strength equivalent to 50% of the base metal. Weld performance could be further improved when using the 0.9-kW, 10-pps weld which attained a strength 75% of the base material. Results reinforce the importance proper process parameters to achieve desired mechanical performance.

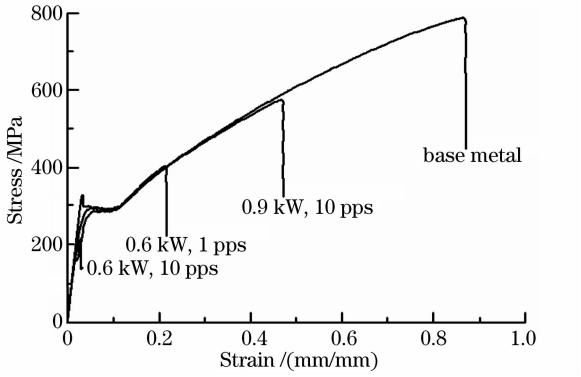

Fig. 8 Effects of laser peak power and pulse width on weld strength and hardness

3.7 Nanojoining of Au Nanopartciles

Figure 9 shows the 1-mmol/L Au nanoparticle solution before and after irradiated at a laser intensity of 4×10^{14} W/cm^2 for 10 min. As-grown Au nanoparticles (before irradiation) have an average size of 15 nm. Two effects have been observed by femtosecond laser irradiation: the generation of large number of tiny nanoparticles with a diameter of 1～3 nm; welding of 2～3 Au nanoparticles with a size around 15 nm. It is reasonable to deduce that these tiny nanoparticles are created by the fragmentation of Au nanoparticles through laser irradiation. A previous study has identified the electron ejection as the first step of photofragmentation by nanosecond laser pulses[35]. This electron emission causes nanoparticles to become positively charged and the repulsion among the charges leads to the fragmentation. Compared with nanosecond laser, the interaction between femsecond laser pulses and matter is dominant by electron ejections and there is little en-

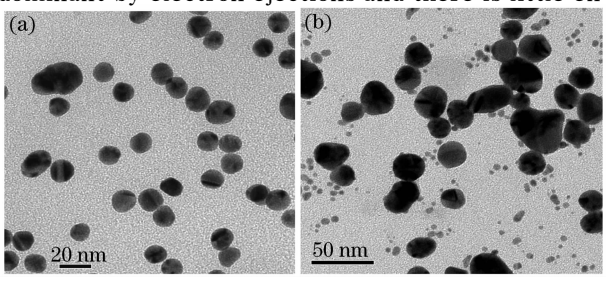

Fig. 9 Effects of Au nanoparticles solution irradiated by focused femtosecond laser pulses. (a) as-grown Au nanoparticles; (b) irradiation

ergy transferring between excited Au electrons and Au lattice[36]. It is thus expected that the effective photofragmentation will occur in femtosecond laser irradiation. It is worth noting that heating-melting-evaporation processes are also observed in nanosecond laser irradiation[37]. It is difficult to attribute such a thermal mechanism to the welding of Au nanoparticles since the thermal coupling time between electrons and lattice is about 1 ps, remarkably longer than the laser pulses. Other mechanisms should take responsible for the present welding by femtosecond laser irradiation.

Figure 10(a) shows the coalescence effect of Au nanoparticles in solution for one month. It is evident that the solid state diffusion leads to partial connection between some nanoparticles. But some particles are not connected even with a very narrow gap. This can be understood that the solid state diffusion rate is anisotropic and thus the joint by solid state diffusion may be controlled by the crystal orientation and relative configurations between two neighbour particles. In contrast, welded nanoparticles by femtosecond laser are extensive. The statistic analysis shows that 70% ~ 80% particles are joined. It is important to point out that as shown in Fig. 10(b), the welding results in a remarkable neck area between two particles with smoothly curved surface while solid state diffusion leads to narrow connect with an acute angle. Thus, solid state diffusion mechanism can be ruled out. A possible mechanism is that the ultrafast melting of Au nanoparticles is due to the interaction between femtosecond laser and Au nanoparticles[2]. Unlike a thermal diffusion mechanism, ultrafast melt of solid can occur after ejection of about 9% bonding electrons[38]. Due to weakening of bonding the solid material starts to melt.

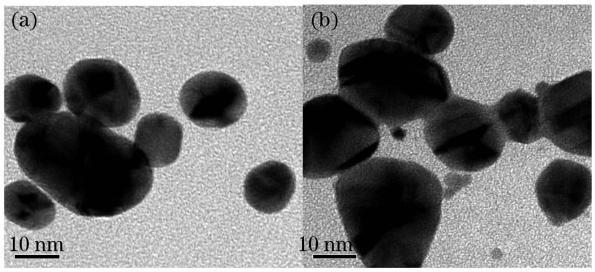

Fig. 10　Coalescence and welding of Au nanoparticles

Figure 11 shows the irradiation effect of femtosecond laser with an intensity of 3×10^{10} W/cm^2. It is clear that the photofragmentation is dramatically

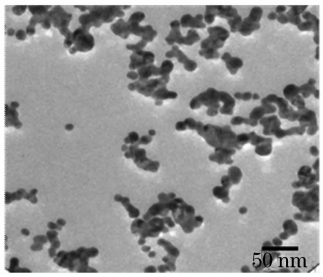

Fig. 11　Welded Au nanoparticles and surface enhanced Raman spectra of irradiated acetone

suppressed while most of nanoparticles are welded together. This is consistent with the welding due to the nonthermal ultrafast melt mechanism. Lowering the laser intensity does not significantly change the electron ejections and thus nanoparticles can still effectively melt. It is difficult to explain the welding with a thermal mechanism since an extremely high laser intensity should not lead to welding rather than the evaporation of most of nanoparticles.

3.8　Nanopatterning of Ag Surfaces

Figure 12 presents the crater generated by focused femtosecond laser with continuing 25 pulses on the Ag surface. It is evident that island structure formed at the bottom of crater. Figure 12(b) exhibits local structures of some islands and the wall of crater. Clearly these areas are covered by regular patterns. These patterns display a spacing of 600~700 nm at the crater wall while widening approaching the center. High magnification SEM imaging shows these microscale patterns are formed by aligned nanoparticles (not shown here). Experiments show that these nanostructures can be created both in air and vacuum. It is notable that such nanostructures are created simply by femtosecond laser irradiation.

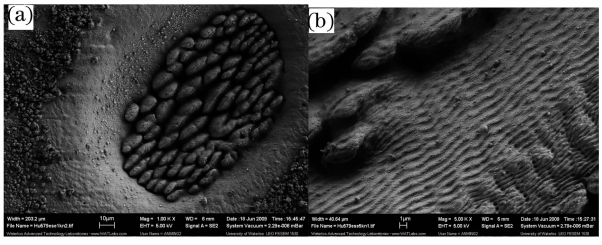

Fig. 12　Irradiated effect of femtosecond laser pulses on Ag surface

Figure 13 illustrates the application of nanopatterns created on Ag surface. The irradiated area is deposited diamond-like carbon films with a thickness of 150 nm with femtosecond pulsed laser abla-

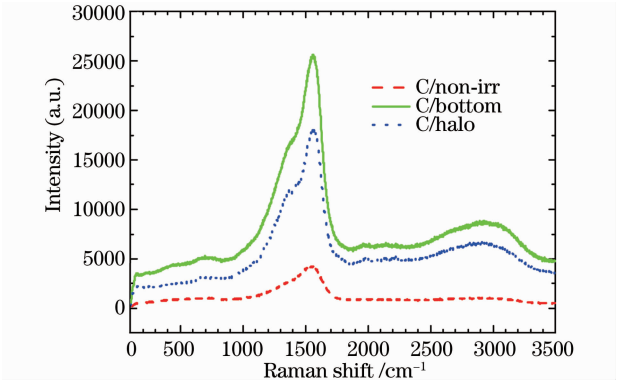

Fig. 13 Raman spectra of carbon deposited on irradiated Ag surface excited with an Ar ion laser at a wavelength of 488 nm

tion. Clear Raman enhancement is observed at the bottom and wall areas, where nanopatterns are created. Such a Raman enhancement can be attributed to the electromagnetic amplification by local surface plasmon excitation[25].

4 Conclusions

In conclusion, recent progresses in laser welding of AHSS for automotives and Pt, Ti, and Nitinol alloys for medical applications, as well as laser nanofabrication are reviewed. Al interlayer enhances the weldability of galvannealed AHSS. Mechanical performance of AHSS weldment is controlled by the movement of local weld line and softening areas. Oxygen, the formation of intermetallic layer, and laser processing parameters are dominant factors governing the mechanical properties of laser microwelding. Femsecond laser irradiation at a proper intensity results in the welding of most Au nanoparticles while avoiding photofragmentation. The nanowelding mechanism is due to nonthermal ultrafast melting of Au nanoparticles. Nanopatterns of Ag can effectively work as the probe for the surface enhanced Raman spectroscopy.

References

1 Y. Zhou. Microjoining and Nanojoining [M]. Woodhead Publishing Ltd, Cambridge, England, CRC Press, 2008

2 A. Hu, M. Rybachuk, Q.-B *et al*.. Direct synthesis of sp-bonded carbon chains on graphite surface by femtosecond laser irradiation [J]. *Appl. Phys. Lett.*, 2007, **91**: 1319061～1319063

3 Y. Zhou, A. Hu, M. I. Khan *et al*.. Recent progress in micro and nanojoining [J]. *J. Phys. Conf. Ser.*, 2009, **165**: 012021～012026

4 International Iron and Steel Institute: Advanced High Strength Steel Application Guidelines, Version 3 Sept 2006, www.worldautosteel.org

5 A. R. Marder. The metallurgy of zinc-coated steel [J]. *Prog. in Mater. Sci.*, 2000, **45**: 191～271

6 Auto/Steel Partnership: Tailor welded blank design and manufacturing manual, Technical Report, 1995

7 D. Dry, W. Wadell, D. R. J. Owen. Determination of laser weld properties for finite element analysis of laser welded tailored blanks [J]. *Sci. Technol. Weld. Joining*, 2002, **7**: 11～18

8 S. K. Panda, D. Ravi Kumar, H. Kumar *et al*.. Characterization of tensile properties of tailor welded IF steel sheets and their formability in stretch forming [J]. *J. Mater. Process. Technol.*, 2007, **183**: 321～332

9 C. H. Cheng, M. Jie, L. C. Chan *et al*.. True stress-strain analysis on weldment of heterogeneous tailor welded blanks- a novel approach for forming simulation [J]. *Int. J. Mech. Sci.*, 2007, **49**: 217～229

10 E. L. Baardsen. Method of welding galvanized steel [P]. U. S. Patent 3,969,604, 1976, 13

11 N. Karube, Y. Nakata, A. Mori. Proceedings of the 25th ISATA International Symposium on Automotive Technology and Automation, Florence, Italy, 1992 _Automative Automation Ltd., Croydon, UK_,119～137

12 A. Dasgupta, J. Mazumder, M. Bembenek. Proceedings of ICALEO 2000, Symposium on Laser Applications in the Automotive Industry, Laser Institute of America, Orlando, FL, 2000, pp. A-38～A-45

13 R. R. G. M. Pieters, R. Thiessen, I. M. Richardson, Laser welding of zinc coated steel in an overlap configuration. IIW Document IV-838-03. Inter. Inst. of Welding, Paris, France, 2003

14 X. Li, J. Xie, Y. Zhou. Effects of oxygen contamination in the argon shielding gas in laser welding of commercially pure titanium thin sheet [J]. *J. Mater. Sci.*, 2005, **40**: 3437～3443

15 N. J. Noolu, H. W. Kerr, Y. Zhou *et al*.. Laser weldability of Pt and Ti alloys [J]. *Mater. Sci. Eng. A*, 2005, **397**: 8～15

16 M. I. Khan, S. K. Panda, N. Zhou. Effects of laser welding parameters on the mechanical properties of Ni-50.7 wt% Ti [J]. *Mater. Trans.*, 2008, **49**: 2702～2708

17 T. Terrones, F. Banhart, N. Grobert *et al*.. Molecular junctions by joining single-walled carbon nanotubes [J]. *Phys. Rev. Lett.*, 2002, **89**: 075501-1-4

18 B. Wei, R. Vajtai, P. M. Ajayan. Reliability and current carrying capacity of carbon nanotubes [J]. *Appl. Phys. Lett.*, 2001, **79**: 1172～1174

19 C. Chen, L. Yan, E. S. Kong *et al*.. Ultrasonic nanowelding of carbon nanotubes to metal electrodes [J]. *Nanotechnology*, 2006, **17**: 2192～2197

20 P. J. de Pablo, E. Graugnard, B. Walsh *et al*.. A simple, reliable technique for making electrical contact to multiwalled carbon nanotubes [J]. *Appl. Phys. Lett.*, 1999, **74**: 323～325

21 W. II Park, J. S. Kim, G. Yi *et al*.. Fabrication and electrical characteristics of high-performance ZnO nanorods field-effect transistors [J]. *Appl. Phys. Lett.*, 2004, **85**: 5052～5054

22 C. O. Girit, A. Zettl. Soldering to a single atomic layer [J]. *Appl. Phys. Lett.*, 2007, **91**: 1935121-4

23 E. Ide, S. A. Hirose, K. F. Kobayashi. Metal-metal bonding process using Ag metallo-organic nanoparticles [J]. *Acta Mater.*, 2005, **53**: 2383～2393

24 S. J. Kim, D. J. Jang. Laser-induced nanowelding of gold nanoparticles [J]. *Appl. Phys. Lett.*, 2005, **86**: 033112

25 A. Hu, W. W. Duley. Surface enhanced Raman spectroscopic characterization of molecular structures in diamond-like carbon films [J]. *Chem. Phys. Lett.*, 2008, **450**: 375～378

26 M. Xia, Z. Tian, L. Zhao *et al*.. Fusion zone microstructure evolution of Al-alloyed TRIP steel in diode laser welding [J]. *Mater. Trans.*, 2008, **49**: 746～753

27 J. Chen, K. Sand, M. S. Xia *et al*.. Transmission electron microscopy and nanoindentation study of the weld zone microstructure of diode-laser-joined automotive transformation-induced plasticity steel [J]. *Metal. and Mater. Trans A*, 2008, **39**: 593～603

28 S. K. Panda, N. Sreenivasan, M. Kuntz *et al*.. Numerical simulations and experimental results of tensile test behavior of laser

butt welded DP980 steels [J]. *Jnl. Eng. Mater. Technol.* (*Trans. ASME*), 2008, **130**:1～9

29 M. Xia, N. Sreenivasan, S. Lawson *et al*.. A comparative study of formability of diode laser welds in DP980 and HSLA steels [J]. *Jnl. Eng. Mater Technol.* (*Trans. ASME*), 2007, **129**:446～452

30 M. S. Xia, M. L. Kuntz, Z. L. Tian *et al*.. Failure study on laser welds of dual phase steel in formability testing [J]. *Sci. Technol. of Welding and Joining*, 2008, **13**:378～387

31 S. K. Panda, V. H. Baltazar Hernandez, M. L. Kuntz *et al*.. Formability analysis of diode-laser-welded tailored blanks of advanced high-strength steel sheets [J]. *Metal. and Mat. Trans. A*, 2009, **40**:1955～1967

32 S. K. Panda, M. L. Kuntz, Y. Zhou. Finite element analysis of effects of soft zones on formability of laser welded advanced high strength steels [J]. *Sci. Technol. Weld. Joining*, 2009, **14**:52～61

33 A. Hu, J. Sanderson, A. A. Zaidi *et al*.. Direct synthesis of polyyne molecules in acetone by dissociation using femtosecond laser irradiation [J]. *Carbon*, 2008, **46**:1823～1828

34 T. B. Massalski. Binary Alloy Phase Diagrams [M]. ASM International, Materials Park, OH, 1990

35 P. V. Kamat, M. Flumiani, G. V. Hartland. Picosecond dynamics of silver nanoclusters. Photoejection of electrons and Fragmentation [J]. *J. Phys. Chem. B*, 1998, **102**:3123～3128

36 S. Nolte, C. Momma, H. Jacobsm *et al*.. Ablation of metals by ultrashort laser pulses [J]. *J. Opt. Soc. Am. B*, 1997, **14**:2716～2722

37 A. Takami, H. Kurita, S. Koda. Laser-induced size reduction of noble metal particles [J]. *J. Phys. Chem. B*, 1999, **103**:1226～1232

38 P. Stampfli, K. H. Bennemann. Dynamical theory of the laser-induced lattice instability of silicon [J]. *Phys. Rev. B*, 1992, **46**:10686～10692